ACS APPLIED ELECTRONIC MATERIALS

pubs.acs.org/acsaelm Article

Understanding Selectivity Loss Mechanisms in Selective Material Deposition by Area Deactivation on 10 nm Cu/SiO_2 Patterns

Mattia Pasquali, Patrick Carolan, Stefanie Sergeant, Johan Meersschaut, Valentina Spampinato, Thierry Conard, Alessandro Viva, Stefan De Gendt, and Silvia Armini*

Cite This: *ACS Appl. Electron. Mater.* 2022, 4, 1703−1714 Read Online

ACCESS | Metrics & More | Article Recommendations | Supporting Information

ABSTRACT: Area-selective deposition (ASD), a "bottom-up" substrate-selective material deposition process, is a promising solution to overcome the current limitations experienced in semiconductor manufacturing processes, which rely on "top-down" patterning techniques. To achieve this selective material growth, atomic layer deposition (ALD) is frequently employed in conjunction with a blocking layer to suppress material nucleation on the nongrowth areas. ASD is suitable on many levels of wafer manufacturing; notably, its "bottom-up" nature makes it more impactful at the smallest critical dimensions (CDs), such as sub-10 nm. Nevertheless, the ASD studies at such relevant nanoscale dimensions are very limited or nonexistent. Therefore, we studied ASD enabled by 1-octadecanethiol (ODT)-derived self-assembled monolayer (SAM) passivation on unprecedented scaled-down Cu/SiO_2 patterns, targeting ASD of hafnium nitride on 10 nm-wide dielectric spacings. Pulsed force atomic force microscopy nanomechanical characterization proved the tight confinement of the organic layer to the metal lines even on such high-density patterns. In addition, transmission electron microscopy, energy-dispersive X-ray spectroscopy, and scanning electron microscopy (SEM) measurements reveal the selective and conformal deposition of ∼5.0 nm hafnium nitride film on the 10 nm-wide SiO_2 spacings. Nevertheless, it is shown that, as the pattern features shrink, the undesired lateral expansion of the isotropically growing ALD film becomes a more stringent limitation to the ASD resolution. The "monolayer trade-off" associated with the employed passivation to enable ASD is analyzed in this work. In fact, a monolayer-thick blocking film is desired to avoid poisoning of the growth surface, whereas the ASD film lateral expansion could be effectively prevented if thicker passivation films are employed instead.

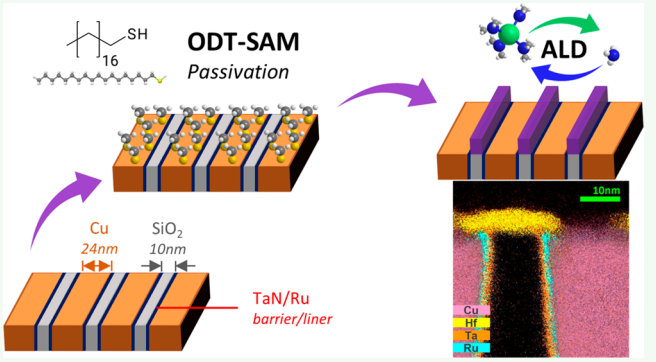

KEYWORDS: *area-selective deposition, atomic layer deposition, self-assembled monolayer, alkanethiol, interfaces*

INTRODUCTION

Nanoscale materials and innovative patterning techniques play a crucial role in enabling sub-5 nm node technologies.[1] Conventional semiconductor manufacturing processes heavily rely on "top-down" lithography and etch steps, which are fated to not meet the ever-increasing requirements for alignment imposed by device miniaturization.[1−3] Commercially available lithographic techniques have a risk of shifting from technology enablers in bottleneck processes in certain steps of device fabrication. Therefore, the never-ending nanoelectronics downscaling has made the semiconductor industry receptive to pioneering nanofabrication methods.[1,4] Among the potential self-aligned patterning schemes, area-selective deposition (ASD) is emerging as a promising solution to tackle such manufacturing challenges by enabling "bottom-up" material deposition on prepatterned substrates.[1,5−9] ASD refers to a material-selective process whereby a target film is deposited exclusively on a certain surface, the growth area (GA), whereas no material nucleation is observed on the nongrowth area (NGA). Hence, ASD is suggested as a key nanofabrication method in a wide range of application fields[3−5,8−10] with semiconductor processing holding the most stringent targets in terms of selectivity, estimated defects below 10^6 cm^{-2},[8,11] and substrate feature dimensions, smaller than ∼10 nm critical dimension (CD).[1]

This confined material growth is most commonly accomplished by exploiting well-distinguished local surface chemistries in conjunction with deposition techniques whose growth rate can be affected by the substrate's chemical specificity.[7,12−14] Therefore, one of the most successful material deposition techniques for ASD applications is atomic layer

Received: December 29, 2021
Accepted: March 15, 2022
Published: March 29, 2022

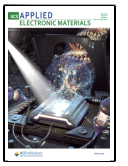

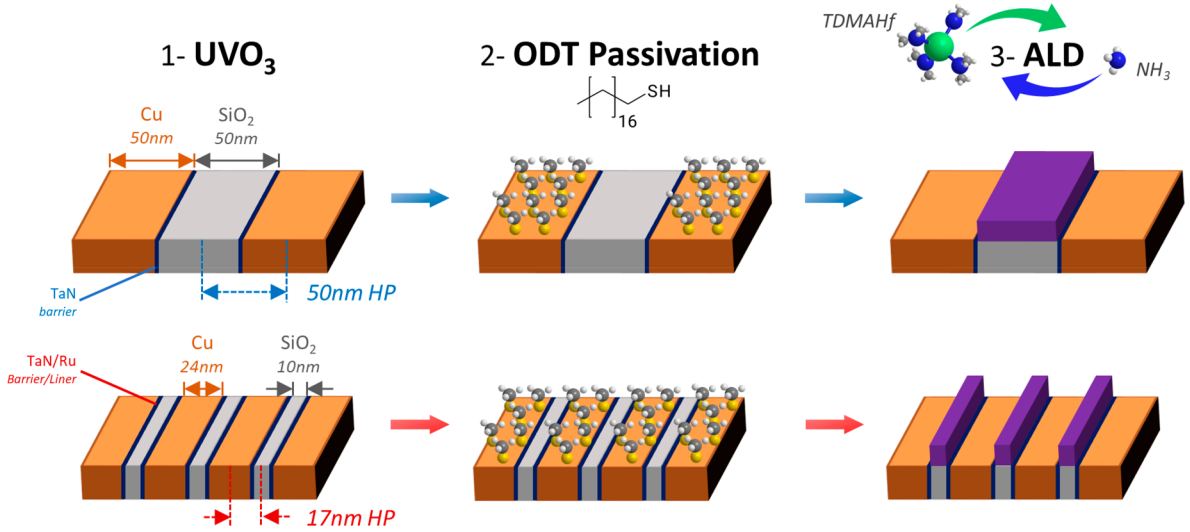

Figure 1. Schematic illustration of the SAM-enabled ASD process on 50 nm half-pitch and 10 nm critical dimension Cu/SiO_2 patterns. Step 1: the substrates are exposed to UV/ozone for 10 min. Step 2: the selective chemisorption of the octadecanethiol-derived SAM is exploited to passivate the Cu lines. Step 3: area-selective hafnium nitride atomic layer deposition is performed.

deposition (ALD), whose well-known surface-dependent nucleation rate relies on the solid−gas self-limiting half-cycle surface reactions.[7,13,15,16] Indeed, on a suitable patterned substrate, it is observed that ALD starts instantly on the GA, whereas a nucleation delay is observed on the NGA, potentially achieving ASD. To enhance the possible intrinsic selectivity offered by the ALD process, a selective surface blocking layer is used to prevent nucleation on the NGA.[9,12,17−23] In these ASD strategies, commonly referred to as area-deactivation schemes, material growth blocking functionalities are either selectively grafted[12,17,18,24−27] or formed by gas/plasma and wet surface treatments.[21,23,28,29]

Self-assembled monolayers (SAMs) fall in the former category and have been used as efficient ASD masks since their introduction in 2005 by Chen et al.[12] SAM precursors exploit a reactive moiety to selectively form chemical bonds with the targeted material surface, whereas their terminal group defines the organic film's surface properties. In ASD mask application, these typically consist of a trimethyl or trifluoromethyl group to prevent ALD precursor physisorption. Moreover, SAM molecules present an alkyl chain that provide the driving force to the self-assembly process through the development of dispersion forces by interchain van der Waals (VdW) interactions.[30] The alkyl backbone impact on the organic film properties explains why relatively long chain precursors, approximately above 11 C atoms, were favored for ASD application.[12,20,31−33] In fact, the longer alkyl chain provides thicker SAMs and favors the molecule's adoption of an all-trans configuration that ultimately results in a high degree of VdW interactions and ensures a close-packing formation.[12,30,31,34]

Clearly, thick and dense SAMs are desirable properties for a blocking layer. Nevertheless, in the last four years,[17] a new class of less bulky organic precursors has gained increasing attention as a candidate for an ASD mask, which includes short chain SAM precursors and small molecular inhibitors (SMIs).[6] Despite the reduced layer thickness and the absence of long alky chains that provide VdW interactions, SMIs offer several advantages. For instance, SMIs can be easily deposited from the vapor phase and hence can be redosed at each ALD cycle, virtually preventing any degradation of the ASD mask during the deposition process.[6,17,25] Moreover, as ASD is targeting aggressively scaled-down patterns and high aspect ratio 3D structures, small molecular size precursors are less likely to interfere with the material nucleation on the growth surface if compared to more bulky SAM monomers.[35]

Despite the relentless development and improvement of ASD during the last two decades, somehow only a few studies have been carried out on relevant nanoscale dimensions for semiconductor manufacturing applications.[20,21,23,24,36,37] Therefore, in this work, we investigate ASD on unprecedently scaled-down patterns with a CD as small as 10 nm (Figure 1). The well-known selective chemisorption of 1-octadecanethiol (ODT) on Cu over SiO_2 is exploited to enable ASD of hafnium nitride by ALD. The proposed ASD scheme is tested on Cu, SiO_2, and TaN homogeneous substrates as well as 50 nm half-pitch (HP) and 10 nm CD Cu/SiO_2 lines. By studying the ODT-enabled ASD strategy on progressively smaller patterns, we shed light on the opportunities and challenges faced by aggressively scaled-down patterns, which are of utmost importance for the ASD applications. Pulsed force atomic force microscopy (AFM) nanomechanical characterization is employed on 10 nm CD structures to visualize and demonstrate the selectivity of the SAM passivation.[38,39] Moreover, this research assesses the feasibility of SAM-based ASD on unprecedented small patterned features, highlighting the critical limitation imposed by the later expansion of the isotropically growing ALD film.

EXPERIMENTAL PROCEDURE

Materials. 300 mm Si wafers were provided by SunEdison Semiconductor. ODT and tetrakis(dimethylamido)hafnium (TDMAHf) were provided by Sigma-Aldrich and used as received. Absolute ethanol was supplied by VWR and used as received.

Substrate Preparation. Every substrate used in the present work was prepared starting from a 300 mm Si wafer. The SiO_2 surface was obtained by exposing the Si wafer to the atmosphere followed by a 10 min exposure to UV/ozone.

Homogeneous TaN substrates were produced by thermally growing 100 nm SiO_2 and depositing 10 nm TaN by physical vapor deposition (PVD). Conversely, to produce nonpatterned Cu samples,

https://doi.org/10.1021/acsaelm.1c01348
ACS Appl. Electron. Mater. 2022, 4, 1703−1714

3 nm PVD TaN was deposited on SiO_2 to ensure a good adhesion between the SiO_2 and the 30 nm PVD Cu seed layer and the metal diffusion barrier. Starting from the seed layer, 500 nm Cu film is deposited via electroplating, followed by a chemical−mechanical polishing (CMP) step, which resulted in a final Cu layer thickness of approximately 200 nm.

Two patterned Cu/SiO_2 structures were used to assess the ASD performance of the ODT passivation: 50 and 17 nm HP substrates (Figure 1). The former consisted of 50 nm Cu and SiO_2 lines/spacings, whereas the latter was made up of 24 nm-wide Cu lines and 10 nm-wide SiO_2 spacing, and thus, it is referred to as the "10 nm CD pattern". The dielectric layer was patterned by lithography. The 50 nm HP structures were patterned by immersion lithography, whereas the 10 nm CD patterns were patterned by extreme ultraviolet lithography.

In both structures, PVD TaN was used as a metal diffusion barrier, 3 and 1.5 nm thick for the 50 and 10 nm CD patterns, respectively. In the latter substrate, 1.5 nm Ru deposited by chemical vapor deposition (CVD) was employed as a liner. Cu was deposited by electrodeposition in an alkaline Cu plating bath, enabled by a 6 nm Cu seed layer previously deposited by PVD. The substrate was then subjected to a 30 s annealing at 180 °C in He/H_2. Finally, CMP was performed to remove the Cu overburden and planarize the stack down to the Cu/SiO_2 lines.

SAM Functionalization. Cu and Cu/SiO_2 patterned substrates were modified with ODT by immersion liquid-phase deposition after CMP. Before being transferred to an inert nitrogen atmosphere, where the SAM deposition was performed, the samples were exposed to 10 min of UV/ozone (*ex situ*). The exposure of the Cu surface to the UV/ozone pretreatment favors the formation of a dense ODT-SAM on Cu, as described in an article previously published by our research group.[40] This surface treatment was also performed on reference substrates not intended to be coated by ODT. The SAM deposition was performed under protective N_2 atmosphere to prevent the ODT solution degradation. Under nitrogen, substrates were submerged into a 50 mM ODT solution in ethanol for 45.8 ± 1.1 h. As the samples were taken out from the coating solution, they were rinsed and sonicated with an excess of ethanol and dried under nitrogen flow. Immediately, the rinsed substrates were sealed and transferred to the ALD chamber. Experiments were designed to minimize the waiting time between sample removal from the SAM solution and ALD process, while samples were stored under a N_2 atmosphere.

Hafnium Nitride ALD. Hafnium nitride ALD was carried out in a Veeco Savannah 300S reactor placed under a nitrogen atmosphere with a reactor temperature in the 65−250 °C range. Sequential pulses of TDMAHf for 0.300 s and NH_3 for 0.025 s with a 30 s intrapulse purge step were used. An initial 180 s temperature stabilization step was performed. As ASD is targeted, the intrapulse purge and temperature stabilization step duration were reduced to 10 and 30 s, respectively. This precaution is taken to reduce the thermal budget experienced by the organic passivation. A nitrogen carrier flow of 20 sccm was employed to deliver the precursors into the reactor. The average precursor partial pressures in the reactor were 0.094 ± 0.012 and 2.085 ± 0.323 Torr during TDMAHf and NH_3 dosing, respectively. The TDMAHf precursor was preheated up to 75 °C, whereas NH_3 was delivered at room temperature.

Film Characterization. The ALD film thickness deposited on SiO_2 was measured by spectroscopy ellipsometry (SE). These *ex situ* measurements were performed using a J. A. Woollam RC2 at 65°, 70°, and 75° incident angles with respect to the substrate normal within 350 and 1000 nm wavelengths with a 5 s acquisition time per angle. The nominal beam diameter was 3 to 4 mm with a divergence of less than 0.4°. In the SE model, the hafnium nitride layer was fitted using a Cauchy layer with the approximation of a constant refractive index within the investigated wavelength range. The fit range of such parameter was limited within the 1.85−2.45 interval.

Rutherford backscattering spectrometry (RBS) was employed to quantify the Hf areal density as hafnium nitride ALD is performed on nonpatterned Cu, SiO_2, and TaN substrates prior to and after a 45.8 ± 1.1 h submersion in an ODT solution.[41] A 1.523 MeV He^+ beam with a beam spot of 1 mm was used. The detector with a full width at half-maximum of 15.1 keV was positioned to define a scattering angle of 170°. The sample normal was tilted at 11° with respect the ion beam, and the sample was rotated along the sample normal during the measurement to avoid channeling effects. The Ta and Hf signals overlap in the RBS spectra. The contribution of the TaN substrate was estimated by the linear regression of the combined Hf and Ta signal intensity as a function of the number of performed ALD cycles (details in the Supporting Information 1). The hafnium nitride film thickness was derived from the Hf areal density by assuming a film density of 1.88×10^{22} Hf atoms/cm^3.

Surface Characterization. Time of flight secondary ion mass spectrometry (ToF-SIMS) was used to detect the presence of SAM molecules on nonpatterned Cu, SiO_2, and TaN prior to and upon a 45.8 ± 1.1 h submersion in an ODT solution. After being taken out from the coating solution, rinsed and sonicated with an excess of ethanol, and dried under nitrogen flow, the samples were sealed under N_2 and transferred to the analysis facility 48 h before the measurements were performed. Both positive and negative ion spectra were recorded with a TOF-SIMS IV instrument from ION-TOF GmbH using a Bi_3^+ gun as the primary source. Although measurements with both polarities had been performed, the negative mode provided the most insightful cluster ions and, therefore, only these ones are discussed in the manuscript. A 150 × 150 μm^2 area was probed at 45° with respect to the normal of the sample. The employed beam energy and current were 25 keV and 0.3 pA, respectively.

Static water contact angle (WCA) measurements were performed on nonpatterned TaN substrates exposed to 10 min of UV/ozone and after 45.8 ± 1.1 h of being dipped in an ODT solution. The *ex situ* measurements were carried out in a DataPhysics Contact Angle System (OCA model) equipped with a CCD camera from Teli and a Hamilton 500 μL syringe with deionized water. The drop volume was fixed to 2 μL and dispensed at 0.5 μL/s. Image fitting was done with SCA20 software using the sessile drop method (ellipse fitting model). ODT-exposed TaN WCAs are measured 24 h after being taken out from the coating solution to allow residual solvent evaporation.

Time-coordinated X-ray photoelectron spectroscopy (XPS) was performed to quantify the ODT concentration on blanket Cu and 50 nm Cu/SiO_2 patterns. A QUANTES instrument from Physical Electronics, employed in Angle Integrated mode, was used to collect XP spectra at a 45° exit angle. The measurements were performed using a monochromatized Al Kα X-ray source (1486.6 eV) and a beam size of 20 μm scanned over an ∼ 60 × 300 μm area. On 50 nm Cu/SiO_2 patterns, the analysis area was identified by recording X-ray induced secondary electron images. Charge neutralization was used during this experiment. Core level binding energies were calibrated against the C 1s binding energy set at 284.8 eV.[42,43] The ODT concentration (Γ_{ODT}) was calculated by comparing the peak intensities of the ODT-related S $2p_{3/2}$, associated with the S−Cu bond doublet centered at 162.7 eV,[42,44] and the respective Cu $2p_{3/2}$ peak of the substrate. The SAM concentration is computed as[45,46]

$$\Gamma_{ODT} = \frac{A_S}{A_{Cu}} \frac{S_{Cu}}{S_S} \rho_{Cu} \lambda_{Cu} \sin(\varphi) \frac{e^{d/(\lambda_S^{ODT} \sin(\varphi))}}{e^{d/(\lambda_{Cu}^{ODT} \sin(\varphi))}} \quad (1)$$

where $\frac{A_S}{A_{Cu}}$ and $\frac{S_{Cu}}{S_S}$ represent the area ratio of the S $2p_{3/2}$ and Cu $2p_{3/2}$ components in the XP spectra and their atomic sensitivity factors, respectively. In eq 1, ρ_{Cu} is the density of Cu atoms in the cuprous oxide surface (∼0.084 mol cm^{-3})[47] and λ_{Cu} denotes the Cu photoelectron inelastic mean-free path (IMPF; ∼0.78 nm) in the substrate,[48] whereas λ_{Cu}^{ODT} and λ_S^{ODT} are the Cu- and S-related photoelectron's IMFP through the carbonaceous film (∼2.12 and ∼3.81 nm, respectively).[45] Finally, d represents the ODT thickness (1.5 ± 0.1 nm),[40] and φ is the exit angle at which the XP spectra were recorded, 45°.

Pulsed force AFM[39] was exploited to obtain 2D topological and nanomechanical property maps of the 10 nm CD patterns prior to and

https://doi.org/10.1021/acsaelm.1c01348
ACS Appl. Electron. Mater. 2022, 4, 1703−1714

upon SAM functionalization. The objective of this analysis is to visualize the ODT passivation on the 24 nm-wide Cu lines 10 nm CD substrate by exploiting the surface adhesion force contrast expected to rise between the passivated metal lines and the hydrophilic SiO_2 areas, analogously to what has recently been shown by our group on 50 nm-wide line structures.[38] For this purpose, a commercial Bruker Dimension Icon AFM system, equipped with a HiRes-C19/Cr-Au probe (0.5 N/m nominal spring constant operated at 2 kHz) and a Si tip (<1 nm radius) from MikroMasch, was used to perform *ex situ* peak force quantitative nanomechanical analysis (QNM).[49] The piezo scanner was controlled by a Bruker Nanoscope V feedback controller, and the experiments were designed to minimize the waiting time between sample processing and the AFM analysis. All adhesion force maps were collected at the same resolution (512 × 512 measurement points) across a 1 × 1 μm scanned area with a pulsed force set point set to 0.150 nN. The adhesion force was defined as the absolute value of the minimum force experienced by the AFM tip during an approach-withdrawn cycle. Nanoscope Analysis v 1.5 software was used to confine the adhesion force distribution analysis to the Cu/SiO_2 lines only (0.644 × 0.406 μm). Distribution fitting and peak deconvolution of the adhesion force were exploited to estimate the ODT coverage (θ_{ODT}) on the 10 nm CD patterns according to the following equation:[38]

$$\theta_{ODT} = \frac{A_{ODT}}{A_{tot}} \tag{2}$$

where A_{ODT} and A_{tot} represent the ODT-related peak subtended area of the bimodal adhesion force distribution and the total subtended area of the fitting function, respectively. These are reported in Supporting Information 2. Distribution fitting and peak deconvolution was done using the Matlab signal processing tool made freely available by Tom O'Haver.[50]

ASD Assessment on Patterns. Top-down scanning electron microscopy (SEM) images of both 50 nm HP and 10 nm CD patterns are taken to study defect formation and evolution during hafnium nitride ALD. A Helios NanoLab 460HP FEI SEM tool was used to collect 1.28 × 0.85 μm images of the patterned substrates upon hafnium nitride deposition using a through-the-lens detector in secondary electron mode with a 10.00 kV applied potential and a probe current varying from 10 to 20 nA. ImageJ software (v 1.52a) was employed to perform brightness and contrast correction to the SEM images as well as to extract the data used to describe defectivity evolution during the ALD process. In this analysis, no ASD film lateral overgrowth at the Cu line edges or defects whose radius is smaller than 2 nm were considered (SEM resolution limit). ASD defectivity on top of the Cu lines was defined by three observables in this work: defect surface fraction (f_{def}), defect density (ρ_{def}), and average defect radius (r_{avg}). The former was defined as the ratio between the total defect area (A_{def}) and the NGA area (A_{NGA}):

$$f_{def} = \frac{A_{def}}{A_{NGA}} \tag{3}$$

whereas ρ_{def} represented the ratio between the number of defects (N_{def}) and A_{NGA}, meaning the number nanoparticles resolved by top-down SEM per unit of area:

$$\rho_{def} = \frac{N_{def}}{A_{NGA}} \tag{4}$$

Finally, r_{avg} was computed from the average defect area (a_{avg}), assuming that the detected nanoparticles had a semispherical shape and, hence, appear circular from a top-down prospective.

$$r_{avg} = \sqrt{\frac{a_{avg}}{\pi}} \tag{5}$$

The errors associated with f_{def} and ρ_{def} were computed by varying the gray scale threshold for defect detection by ±1% with respect to the set value. Conversely, the r_{avg} error is defined as the 25−75% interquartile range of the particle size distribution (PSD). The PSDs were normalized so that their integrals computed over all possible radius values are equivalent to the unit.

Cross-sectional transmission electron microscopy (TEM) images were obtained in conjunction with energy dispersive X-ray spectroscopy (EDS) measurements to assess the ASD quality on 50 nm HP structures and 10 nm CD patterns. The studied cross sections were made using an FEI Helios NanoLab 450HP dual beam focused ion beam (FIB). Prior to the FIB lift-off, the analyzed substrate was coated with three layers in the following order: a thin e-beam Pt layer, a drop-casted organic layer (spin-on carbon) baked at 150 °C, and an ion-beam (30 kV) deposited Pt layer. The cross section was created by milling a trench at 30 kV at either side of the region of interest and attaching it to a lift out needle. Afterward, the cross section was attached to a TEM grid and thinned initially at 30 kV, whereas the final part of the process was performed at 5 kV. At the end, the studied cross sections consisted of a 30−50 nm thick lamella. An FEI Titan^3 G2 60-300 transmission electron microscope operating at 200 kV was employed to collect both TEM images and EDS element maps.

RESULTS AND DISCUSSION

Hafnium Nitride ALD on Homogeneous Surfaces. The hafnium nitride ALD process is initially studied on the growth area of the proposed ASD strategy, thus blanket SiO_2 substrates after 10 min of UV/ozone exposure. The process growth per cycle (GPC) and deposited film's refractive index are investigated by *ex situ* SE as a function of the reactor temperature. The results are reported in Figure 2. A linear relationship is observed between the film thickness and the number of performed deposition cycles throughout the investigated process temperature range (Supporting Information 3). The ALD's GPC at 150 °C measured by SE is corroborated by RBS analysis (Supporting Information 1): the process deposition rate results are 2.0 ± 0.1 and 2.1 ± 0.1 Å/cycles according to the two characterizations, respectively. The SE investigation reveals a dependence of the ALD deposition rate on the reactor temperatures; no clear ALD process window is found within the considered temperatures. The process GPC sits at ∼2.1 ± 0.1 Å/cycles for process

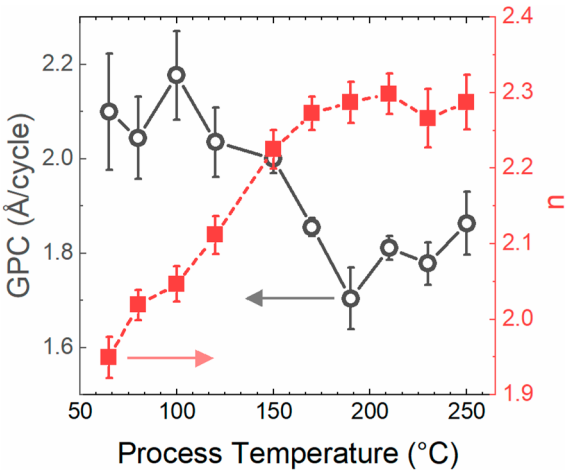

Figure 2. ALD GPC (black) and hafnium nitride refractive index (red) as a function of the process temperature determined by SE measurements. Each GPC data point is computed starting from hafnium nitride thickness measurements upon 10, 20, 30, and 40 ALD cycles, whereas only the last three films are considered as the refractive indexes are determined. ALDs are performed on SiO_2 upon exposure to 10 min of UV/ozone.

https://doi.org/10.1021/acsaelm.1c01348
ACS Appl. Electron. Mater. 2022, 4, 1703−1714

temperatures below 150 °C. Above such a threshold, the hafnium nitride deposition rate decreases and stabilizes at ∼1.8 ± 0.1 Å/cycles. Similarly, the film's refractive index rises with the reactor temperature from ∼1.9 at 65 °C up to ∼2.3 at 170 °C, and no further increase is observed at higher temperatures. The refractive index saturation value is compatible with the values reported in the literature for hafnium nitride with an oxygen content greater than 8%.[51] Both GPC and refractive index trends could be explained by the temperature-dependent ligand-exchange reaction rate between NH_3 and the amido functionalities of the deposited film during coreactant exposure.[52,53] It is suspected that the lower ligand-exchange reaction rate observed at low temperatures leads to a more significant incorporation of methyl-containing TDMAHf functionalities, resulting in a less dense yet thicker hafnium nitride film deposition. Consequently, ALD performed at relatively low temperature, such as below 150 °C, exhibiting higher GPC, and the incorporation of methyl species in the film matrix causes the refractive index to be lower than expected.[51,54,55]

Subsequently, hafnium nitride ALD is investigated on the relevant materials involved in the proposed ASD strategy with an emphasis on understanding the impact of ODT exposure on ALD nucleation on the various surfaces. This purpose is fulfilled by comparing the amount of hafnium nitride deposited on Cu, SiO_2, and TaN substrates and the quantity deposited on the same surfaces after being dipped in ODT solution for 45.8 ± 1.1 h. RBS is employed to quantify the Hf areal density upon 50 hafnium nitride ALD cycles at 150 °C, and the results are reported in Figure 3. As it can be inferred from the results

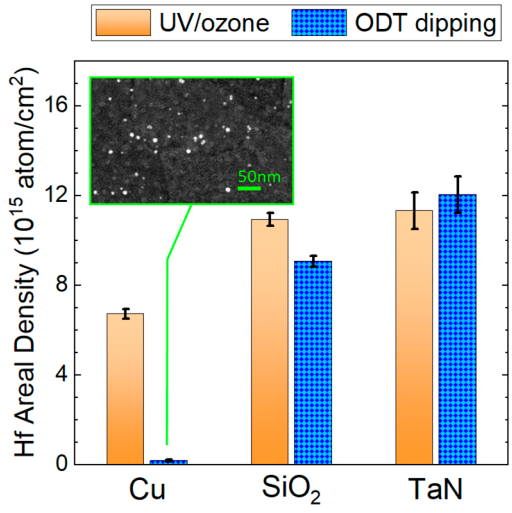

Figure 3. RBS-derived Hf areal density upon 50 hafnium nitride ALD cycles performed on Cu, SiO_2, and TaN exposed to 10 min of UV/ozone (orange) and after 45.8 ± 1.1 h of dipping in ODT (blue). The depositions are carried out at 150 °C. Inset: a top-down SEM image of the ODT-coated Cu upon hafnium nitride ALD (a larger portion is reported in Supporting Information 4).

reported in Figure 3, the ODT passivation significantly inhibits the ALD nucleation exclusively on the Cu surface. Indeed, as the metallic substrate is modified with the ODT passivation, the Hf detected by RBS upon 50 hafnium nitride ALD cycles drops from 6.8 ± 0.2 × 10^{15} to 0.7 ± 0.5 × 10^{14} at·cm^{-2}. This is in great agreement with the numerous literature studies showing the formation of densely packed thiol-derived SAM on Cu.[34,40,46,56−58]

Conversely, no significant material deposition hindering is observed on both SiO_2 and TaN surfaces after submersion in the SAM solution. Nevertheless, as SiO_2 is considered, approximately 10% less Hf is detected after performing 50 ALD cycles if the substrate is previously immerged in the ODT solution compared to unexposed SiO_2. This material deposition delay could be caused by undesired thiol molecule physisorption on the dielectric surface. Nevertheless, no ODT-specific ions, such as $C_{18}H_{37}S^-$, are detected above noise level by ToF-SIMS as SiO_2 is exposed to the SAM solution (Supporting Information 5). Possibly, substrate exposure to high vacuum during the ToF-SIMS may have depleted such physiosorbed species, making it impossible to properly assess their presence with a vacuum technique.

Finally, no significant SAM-related ALD inhibition is observed on TaN. This suggests that no stable ODT passivation is formed on such a material, arguably because of a weak thiol−Ta interaction or the presence of too strong of a Ta−N bond. To support this claim, WCAs are measured on TaN substrates prior to (55.0 ± 1.2°) and upon immersion in the coating solution (55.3 ± 0.7°). The unaltered WCA value after substrate exposure to the ODT solution indicates that no SAM forms on TaN. The impossibility to form a dense thiol−SAM on this material is corroborated by comparing the ODT-specific ion counts (i.e., $C_{18}H_{37}S^-$) on Cu and TaN by ToF-SIMS measurements (Supporting Information 5). After a 45.8 ± 1.1 h immersion in ODT solution, the $C_{18}H_{37}S^-$ intensity is more than 2 orders of magnitude lower on TaN with respect to Cu. Similar conclusions were drawn by Liu et al. as dodecanethiol (DDT) SAM deposition by vapor phase is attempted on TaN substrates.[59]

In summary, according to the RBS analysis on Cu, SiO_2, and TaN, the ODT passivation significantly delays ALD nucleation exclusively on Cu. As 50 hafnium nitride ALD cycles are performed on SiO_2, the exposure to the coating solution causes only a minor change in the Hf areal density detected by RBS from 10.9 ± 0.2 × 10^{15} to 9.1 ± 0.3 × 10^{15} at·cm^{-2}. The poor thiol−Ta chemical affinity results in no ALD blocking observed on TaN, which would have been desirable to more effectively confine the dielectric ASD to the SiO_2 lines.[1,5]

ASD on 50 nm Patterns. ASD is first studied on patterns consisting of 50 nm-wide Cu/SiO_2 lines. The initial focus of the experimental work is to identify the most suitable ASD conditions in term of process temperature. Therefore, ODT-passivated Cu/SiO_2 50 nm HP structures are exposed to hafnium nitride ALD at 100, 120, and 135 °C, followed by top-down SEM analysis to assess the ASD quality. This temperature range is selected according to ODT-SAM thermal stability on 50 nm Cu patterns.[38] The observed defectivity is described in terms of f_{def}, ρ_{def}, and r_{avg}, and their evolutions upon increasing number of performed ALD cycles are presented in Figure 4a.

A portion of the SEM images that correspond to each data point are available in Supporting Information 6. As it can be inferred from Figure 4a, the deposition temperature plays a role of paramount importance in controlling defectivity on the NGA with lower process temperature (i.e., 100 °C) being beneficial for ASD. If hafnium nitride ALD is carried out at 100 °C, the fraction of GA covered with hafnium nitride nuclei remains below 11% after performing 60 ALD cycles (Figure 4a), whereas Cu line closure due to undesired ALD nucleation

https://doi.org/10.1021/acsaelm.1c01348
ACS Appl. Electron. Mater. 2022, 4, 1703−1714

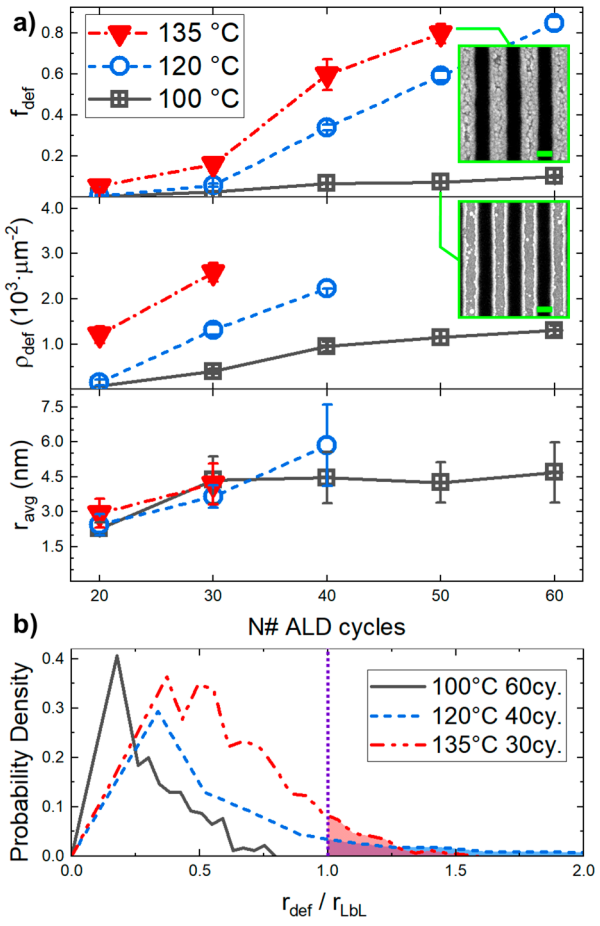

Figure 4. (a) Defect surface fraction (f_{def}), density (ρ_{def}), and average radius (r_{avg}) evolution with increasing number of hafnium nitride ALD cycles performed at 100, 120, and 135 °C on 50 nm-wide Cu/SiO_2 lines. The investigated ALD processes deposit from ~4.0 nm (20 cycles at 135 °C) up to ~13.6 nm (60 cycles at 100 °C) hafnium nitride on blanket SiO_2. Insets: 50 nm pattern top-down SEM images (50 nm scale bar) upon 50 ALD cycles at 100 (bottom) and 135 °C (top). (b) PSDs computed from the 50 nm HP structure exposed to 60, 40, and 30 ALD cycles performed at 100, 120, and 135 °C, respectively. These are plotted as a function of the ratio between the defect radius (r_{def}) and the maximum radius expected from an ideal layer-by-layer growth regime (r_{LbL}). The distribution's filled area represents the nanoparticle fractions that exceed this size threshold.

already becomes dominant after 30 and 40 ALD cycles at 120 and 135 °C, respectively. Because of the film closure of the metal lines, it is impossible to calculate the r_{avg} and ρ_{def} at this ALD stage.

Nevertheless, the SEM analysis reveals that the superior selectivity appreciated at 100 °C is attributed to both a lower defect nucleation rate and hindered nanoparticle growth if compared to higher temperature processes (Figure 4a). If ASD processes at 120 and 135 °C are considered, the defect generation rates are comparable, 104 ± 15 and 138 ± 39 defect per cycle per μm^2, respectively. Nevertheless, at 100 °C, the defect generation rate drops significantly to 31 ± 9 defect per cycle per μm^2. The defect formation rate temperature dependence is in agreement with the thermally activated ODT degradation on Cu observed by pulsed force AFM in a recently published work from our research group.[38] At temperatures as high as 120 °C, a quick depletion of the ODT molecules reveals more of the underneath Cu area, providing a favorable surface to unwanted ALD nucleation. In contrast, the SAM molecule concentration was shown to remain almost unaltered throughout 60 ALD cycles at 100 °C, allowing the effective suppression of the generation of defects. A similar overall trend between process temperature and r_{avg} is observed. The hafnium nitride nuclei appear to grow rapidly as ALD is carried out at 120 and 135 °C, whereas the defect average size remains almost constant with increasing ALD cycles at 100 °C. The lower defectivity observed at the lowest process temperature could be attributed to different phenomena, starting with the higher stability of the SAM film at 100 °C with respect to 120 and 135 °C. As shown in a previously published study from our research group,[38] the ODT concentration on the 50 nm-wide Cu lines remains constant throughout ASD only at 100 °C. Therefore, the highly concentrated alkyl chains surrounding a given defect may make it less likely for gas-phase ALD reactants to reach the nuclei surface due to steric hindrance. This "screening effect" is expected to not be as efficient at 120 and 135 °C than at 100 °C because of faster ODT molecule depletion at such temperatures.

One additional contribution to the faster nanoparticle growth at 120 and 135 °C temperatures is suggested by the PSDs at the latest insightful stage of the ASD process (Figure 4b) before the coalescence of the hafnium nitride layer occurs on the Cu surface. If a given nanoparticle grows only by direct material deposition then, on the basis of geometrical considerations, its radius is expected to increase at a rate equal to the ALD's GPC. In this scenario, defects are considered to grow in a layer-by-layer regime. Therefore, the radius of a certain nanoparticle (r_{def}) cannot exceed the value predicted by ALD's layer-by-layer growth mechanism (r_{LbL}), which corresponds to the thickness of the ASD film. As it can be inferred from the PSD reported in Figure 4b, if hafnium nitride is deposited at 100 °C, no defect exceeds such a threshold (i.e., $r_{def}/r_{LbL} > 1$), providing no evidence of a growth mechanism different than direct material deposition by ALD. Conversely, a non-negligible portion of the PSDs upon ALD at 120 and 135 °C comprise nanoparticles whose radius is greater than r_{LbL} (Figure 4b, filled areas). This ~5% of the total defect suggests that additional growth mechanisms have played a role at 120 and 135 °C. A plausible explanation to this defect overgrowth may rely on the surface diffusion of adspecies and nanoparticles.[36,60−64] The enhanced mobility of such species at higher temperature cause a beyond layer-by-layer expansion of the nanoparticles either by enabling the chemisorption of additional physisorbed precursor or by favoring defect coalescence upon collision. These surface diffusion-driven phenomena agree with the reported experimental observations that defect overgrowth is more significant at higher deposition temperatures.

SEM inspection of the 50 nm HP reveals that ODT offers different inhibition performances on homogeneous and patterned Cu substrates. The poorer ALD blocking of the ODT on the pattern's features, compared to SAM-on-blanket Cu, is highlighted by the SEM analysis. A portion of these images, corresponding to ODT-passivated blanket Cu upon 50 ALD cycles at 150 °C and after 50 hafnium nitride cycles at 135 °C on 50 nm Cu/SiO_2 patterns, are reported in Figure 3 (inset) and Figure 4 (top inset), respectively. The SEM inspection reveals the formation of sparse ALD defects upon 50 ALD cycles at 150 °C on blanket Cu, whereas the same amount of ALD cycles at 135 °C causes an almost full coating

https://doi.org/10.1021/acsaelm.1c01348
ACS Appl. Electron. Mater. 2022, 4, 1703−1714

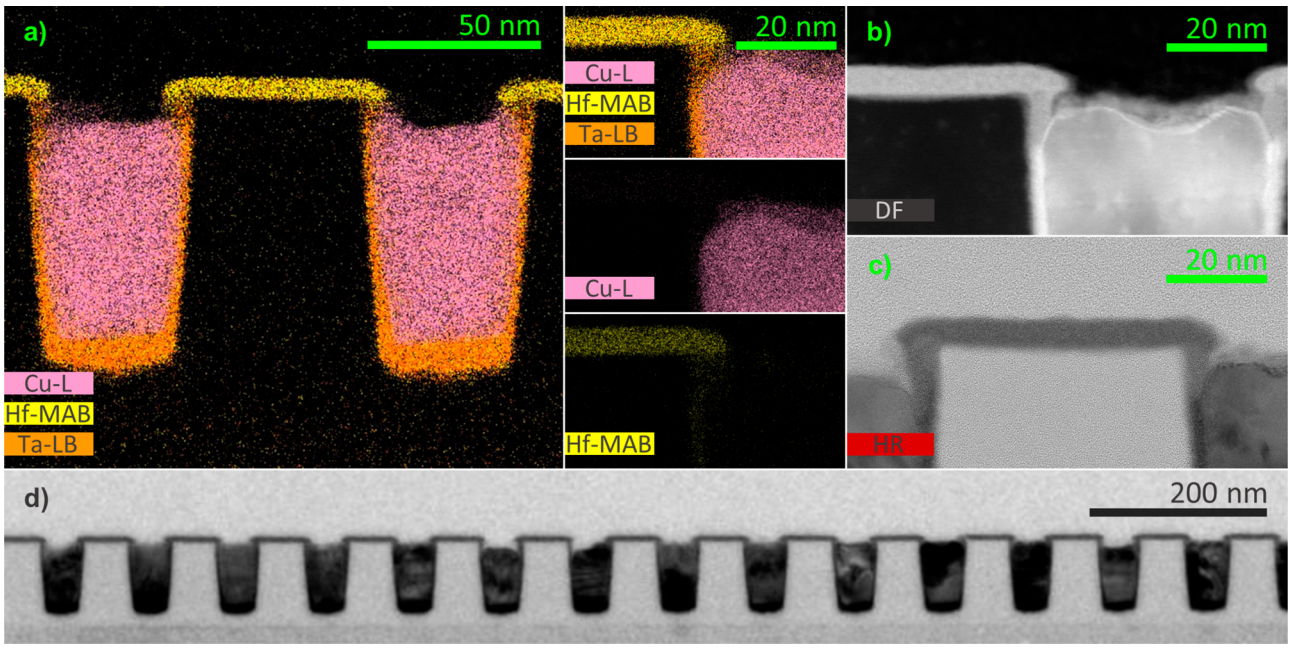

Figure 5. EDS spectral image of the ODT-passivated 50 nm-wide Cu/SiO_2 line cross-section upon 40 hafnium nitride ALD at 100 °C (a). Single element EDS images from Cu-L_α, Hf-$M_{\alpha\beta}$, and Ta-L_β emissions are reported. Cross-sectional DF-TEM (b), HR-TEM (c), and TEM (d) images of the same substrate.

of the 50 nm-wide Cu line with the nitride film. XPS-derived ODT concentration is measured on both blanket and 50 nm patterns, revealing that the molecular concentration of the SAM is significantly higher on the former substrate, 3.10 ± 0.11 molecule/nm^2, compared to the 2.45 ± 0.19 molecule/nm^2 observed on the 50 nm-wide Cu lines.[38] The lower density of the ODT layer may be responsible for the poorer ALD inhibition performances on such patterned features. Moreover, the lower concentration of the SAM molecule indicates lower degree alkyl chain VdW interactions[31] that could lead to a lower degree of stabilization of the ODT molecules during the ASD process. The different molecular concentrations of the organic film on the homogeneous surface and patterns may have been caused by subtle chemical and/or morphological differences among the two Cu substrates. Arguably, "edge effects" on the heterogeneous surface, like the one reported by Chopra et al. on 3D structures,[65] can contribute to the formation of a SAM with a lower degree of crystallinity. This lower level of organization allows the accommodation of a fewer ODT molecules, thus favoring the nucleation of ALD nanoparticles at an earlier stage of the ASD process with respect to a more crystalline SAM. Such discrepancies between the ODT performances on blanket and patterned substrates highlight the critical importance of investigating ASD processes at technology-relevant CDs.

The ASD resolution achieved on the 50 nm HP structure is assessed by EDS measurements taken in conjunction with cross-sectional TEM. On the basis of the SEM analysis (Supporting Information 6), the substrate undergoing 40 hafnium nitride ALD cycles at 100 °C is selected for TEM and EDS inspection, and the results are presented in Figure 5. The investigation shows that ∼6.5 nm hafnium nitride film is selectively deposited on the 50 nm SiO_2 spacings. This ASD performance is observed throughout the whole 50 nm HP (Figure 5d), highlighting the repeatability of the proposed ASD scheme. As revealed by the EDS cross-section images (Figure 5a), no Hf is detected on Cu, whereas top-down SEM reveal sparse particles on the NGA (Supporting Information 6). This points to the value of combining relatively large-field characterizations (e.g., SEM images) along with TEM/EDS as the process selectivity is assessed. All the analyzed SiO_2 spacings are fully coated by the hafnium nitride film.

TEM/EDS analysis shows that ALD nucleation is unaffected on top of the TaN barrier. This agrees with the poor passivation properties exhibited by the ODT layer on TaN, as shown by the RBS analysis presented in Figure 3. Moreover, the ASD film appears to marginally protrude from the TaN barrier and extend over the very edge of the Cu lines. At the best of the TEM and EDS resolution, no hafnium nitride nucleation is observed directly on the Cu edges. This ASD lateral overgrowth, also referred to as a "mushroom" or "cauliflower effect", is a rather well-known consequence of the ALD isotropic growth character.[66] It is challenging to accurately quantify the ASD film lateral protrusion because of the line edge roughness (LER) of the nitride film, which is observed in the top-down SEM images. Such a LER suggests a low degree of reorganization of the ALD film, which is possibly attributed to the low process temperature. Nonetheless, the ASD film undesired lateral expansion over Cu varies between approximately 2 and 4 nm. Therefore, the film lateral overgrowth is marginal compared to the pattern's feature size (i.e., 50 nm), making it a nonrelevant issue as ASD is employed at this scale.

SAM Characterization on 10 nm CD Patterns. The SAM passivation on 10 nm CD structures is characterized by pulsed force AFM.[67−70] The scope of this analysis is to monitor the organic passivation and estimate its surface coverage prior to ALD.[38] The quantification of the surface fraction functionalized by the SAM is information of the utmost importance for ASD on a technology-relevant pattern scale. Undesired shadowing caused by the organic passivation can potentially prevent ALD nucleation on the GA because of

https://doi.org/10.1021/acsaelm.1c01348
ACS Appl. Electron. Mater. 2022, 4, 1703−1714

the blocking layer protrusion over the growth surface. As the dimensions of the area targeted by the ALD shrinks, like the 10 nm-wide SiO_2 spacing considered in this study, potential masking effects are more detrimental due to the reduced dimensions of the substrate's features. The adverse possibility of the SAM-mediated masking effect is indeed one of the reasons that is driving the scientific community to consider smaller sized molecules for passivation purposes.

To monitor the SAM confinement to the GA by pulsed force AFM, the attention is drawn to the analyzed substrate's adhesion force properties evolution prior to and upon the ODT coating. This metrology was recently proved successful on 50 nm HP structures,[38] and it is here tested on aggressively scaled-down 10 nm CD patterns. The adhesion force images collected prior to and upon ODT passivation are reported in Figure 6a, along with the adhesion force distribution (Figure 6b). The full adhesion force images from both samples are available in Supporting Information 2, where the analysis areas used to compute the distributions are shown in Figure 6b. These adhesion force distributions show that, as the SAM is grafted to the metal lines, the initial symmetrical adhesion force distribution turns bimodal with different peak heights, highlighting the formation of two well-distinguished regions exhibiting higher and lower adhesion force. The adhesion force maps upon ODT passivation (Figure 6a) reflect the expected surface chemistry, consisting of bright CH_3-terminated hydrophobic lines of the passivated metal (i.e., low adhesion force) and dark hydrophilic SiO_2 regions (i.e., high adhesion force). This map reveals a 0.2−0.3 nN adhesion force contrast between passivated metal lines and dielectric spacings. On the contrary, prior to the organic layer deposition, the substrate adhesion force results are homogeneous throughout the whole Cu/SiO_2 line structure. In this case, no clear contrast is identified, and the symmetrical Gaussian-shaped adhesion force distribution contradicts the sample geometry, which consists of 24 nm-wide Cu and 10 nm-wide SiO_2.

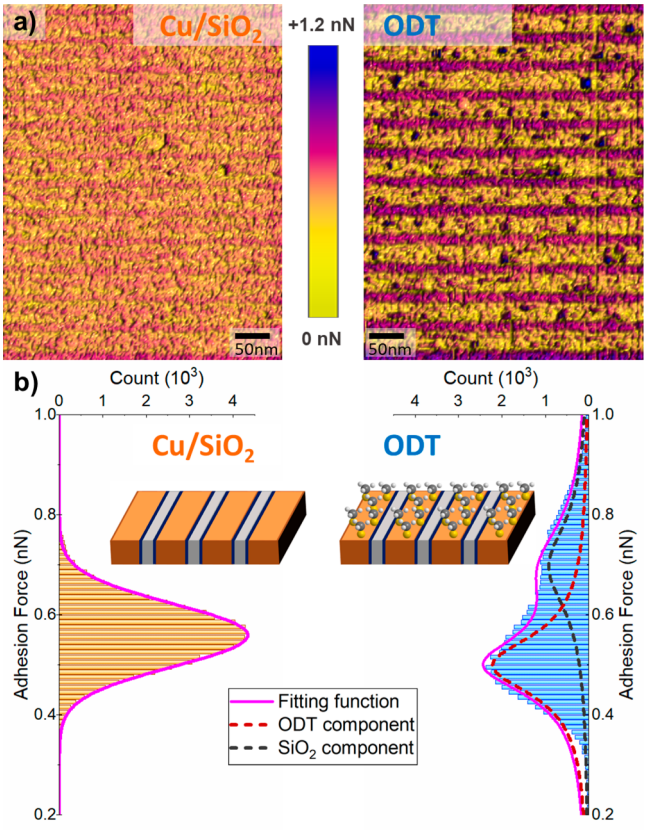

Figure 6. Adhesion force maps of the 10 nm CD Cu/SiO_2 pattern (a) after UV/ozone exposure (left) and upon ODT coating (right) measured by pulsed force AFM. The distributions of such adhesion forces (b) are reported before (left) and after (right) SAM passivation and are plotted within the 0.2−1.0 nN range with a 10 pN quantization interval.

Quantitative insights over the ODT passivation are obtained by further analyzing the 10 nm CD pattern's adhesion force distribution upon SAM modification (Figure 6b). Starting from the cross-sectional images reported in Figure 7, *vide infra*, the surface fraction to undergo the thiol-mediated functionalization is expected to be approximately ∼0.61 with the remaining area, consisting of SiO_2 spacings and the TaN/Ru barrier/liner, left uncoated. As the ODT-passivated substrate's adhesion force distribution (Figure 6b) is deconvoluted into its lower and higher adhesion force components (fitting parameters and results available in Supporting Information 2), a SAM surface coverage equal to 0.63 ± 0.03 is computed according to eq 2. Thus, the nanomechanical characterization performed on the ODT-modified substrate confirms that the organic functionalization occurs exclusively on the metallic surface. On the basis of these insights, no ODT-SAM mediated masking effects of the SiO_2 spacing are expected upon ALD.

ASD on 10 nm CD Patterns. The ASD quality on 10 nm CD patterns is assessed by SEM and EDS measurements in conjunction with cross-sectional TEM. On the basis of the learning from the 50 nm HP structures, hafnium nitride ASD is tested at 100 °C on 10 nm CD Cu/SiO_2 patterns. The results of the TEM, EDS, and top-down SEM analyses on the ODT-passivated samples upon 30 hafnium nitride ALD cycles are presented in Figure 7. From the TEM images, it is concluded that the effective suppression of hafnium nitride nucleation is achieved on Cu, resulting in successful ASD. The ODT-mediated ALD inhibition appears remarkably effective at the central region of the metallic lines. Indeed, according to the top-down SEM image in Figure 7e, almost no ALD nuclei are formed at the center of the Cu lines. The TEM and EDS analyses reveal the deposition of an ∼5.0 nm hafnium nitride continuous layer on the SiO_2 spacings. Despite the CD of the GA being reduced to 10 nm, the ODT passivation does not interfere with the nucleation of the ALD film on SiO_2; both TEM and SEM analyses reveal fully coated dielectric spacings by the ALD film. This is in agreement with the tight confinement of the SAM on Cu suggested by the pulse-force AFM investigation.

Similarly to ASD on 50 nm HP structures, the TEM inspection of the 10 nm CD patterns shows that the ASD film protrudes from the TaN barrier over Cu. The later overgrowth of the nitride film approximately extends for 1 to 4 nm over the metal lines. It is not straightforward to compare the lateral expansion of the ASD film on 50 and 10 nm patterns because of the hafnium nitride relevant LER. Nevertheless, this "mushroom effect" is more detrimental on smaller patterns, since analogous later overgrowth takes over a large fraction of the GA on more scaled-down substrates. As the proposed ASD strategy is considered, despite the nitride lateral overgrowth being comparable on both patterns, 92% to 84% of the Cu surface is available after ASD on the 50 nm HP substrate, whereas only 87% to 67% of the metal lines is not affected by

https://doi.org/10.1021/acsaelm.1c01348
ACS Appl. Electron. Mater. 2022, 4, 1703−1714

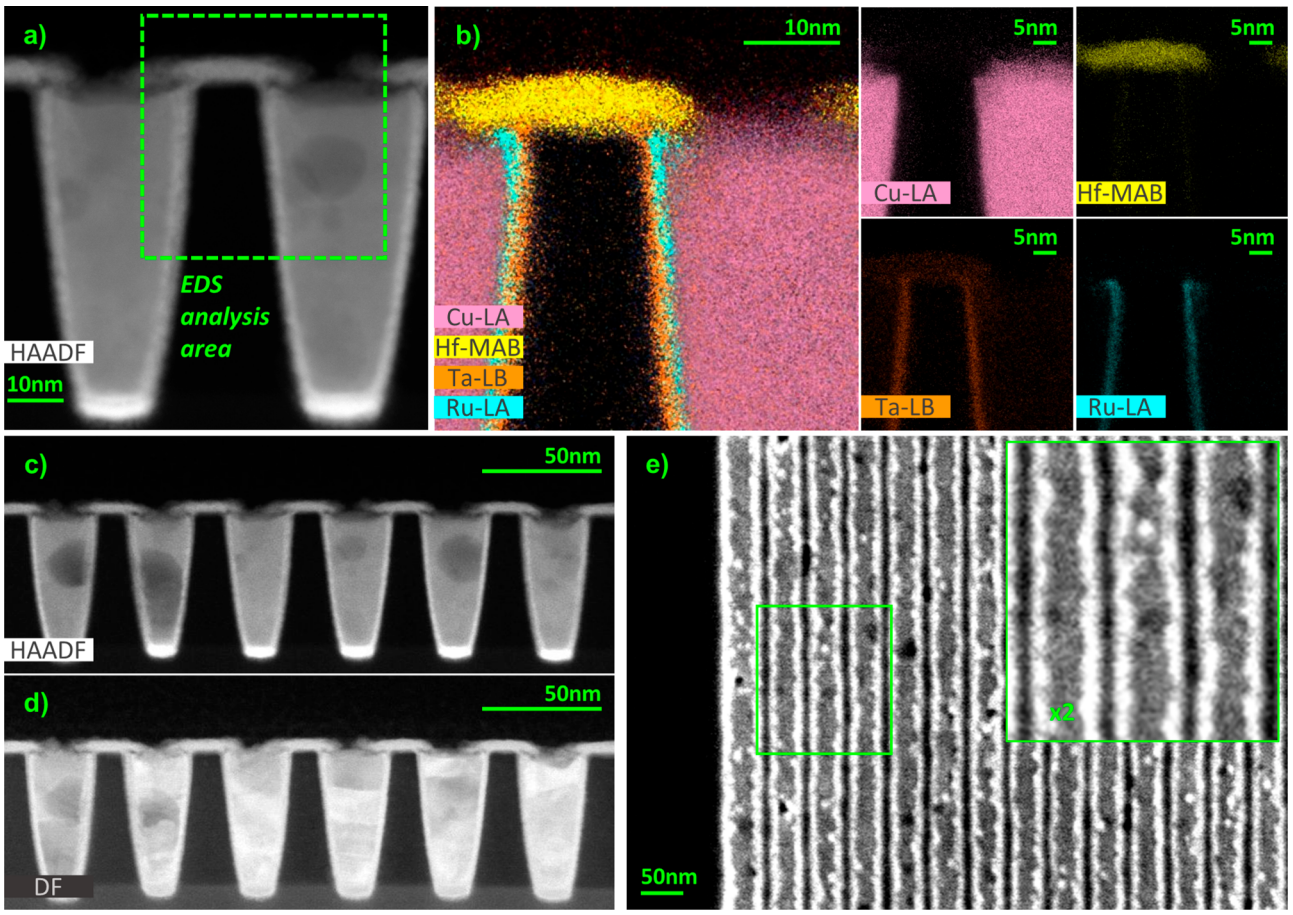

Figure 7. HAADF-TEM (a, c) and DF-TEM (d) images of the ODT-passivated 10 nm CD Cu/SiO_2 pattern upon 30 hafnium nitride ALD cycles at 100 °C. EDS spectral images (b) of the highlighted area in (a) from Cu-L_α, Hf-$M_{\alpha\beta}$, Ta-L_β, and Ru-L_α emissions. Single EDS elemental maps for Cu-L_α, Hf-$M_{\alpha\beta}$, Ta-L_β, and Ru-L_α emissions are reported. Top-down SEM image of the same structure (e); inset: a 2× magnification of the area highlighted in green is presented.

the later expansion of the ALD film on the 10 nm CD pattern. In addition, the SAM inability to passivate the TaN/Ru complex is more disadvantageous at smaller CDs because barriers and liners cannot be scaled-down along with the pattern's lines and spacings.

"Monolayer Trade-off". The presented experimental work highlights the crucial role of the monolayer nature of the passivation layer as ASD is targeted at smaller and smaller CDs, revealing critical insights regarding the investigated passivation layers for ASD purposes. The monolayer thickness of the organic film upon the proposed ODT deposition technique on blanket Cu was reported in a previous study published by our research group.[40] In addition, AFM height scans on 50 nm-wide Cu lines patterns prior to ALD, available in Supporting Information 7, reveal that the SAM preserves its monolayer nature on such patterns (~2.0−2.5 nm).[31] Resolution limits of analogue measurements performed on the 10 nm CD patterns preclude one from calculating the SAM thickness on such structures. Nevertheless, on such patterns, no multilayer thick complexes are detected, strongly indicating that the ODT-SAM adopts a configuration close to the one of the monolayer (Supporting Information 7). As unraveled by the pulse force AFM nanomechanical characterization (Figure 6), even a relatively long alkyl chain SAM monomer, such as ODT, forms a blocking layer that is confined to the NGA. Consequently, no ALD nucleation hampering is observed at the Cu/SiO_2, as demonstrated by the TEM/EDS analysis performed on 10 nm CD patterns upon 30 hafnium nitride cycles (Figure 7). These findings agree with Liu et al.'s work,[59] where the benefit of a truly monolayer-thick DDT-SAM to prevent detrimental masking effects is highlighted using the example of a 50 nm-wide SiO_2 growth surface. In this study, such specific findings are extended to 10 nm-wide SiO_2 spacings using a bulkier thiol precursor. Moreover, for the first time, the proof of the SAM confinement to such scaled-down Cu lines is provided.

Therefore, the results presented in this Article shed new light on long chain SAM precursors for ASD applications. In fact, a relatively bulky precursor, such as ODT, provides ASD masks that are tightly confined to the NGA, thus preventing the creation of ALD-free patches on the GA upon material deposition. Under the right deposition conditions, long chain SAMs still represent suitable blocking layers for ASD applications, as no selectivity issue is observed on 10 nm patterns. Regarding relevant 3D structures, such as high aspect ratio trenches, to the best of the authors' knowledge, no manuscript has reported masking of the GA caused by a long chain SAM.

Despite the great selectivity of the ALD inhibition exhibited by the ODT-SAM, a critical issue is observed at technology-relevant pattern scale: the lateral overgrowth of the ASD film. This is a well-known and not yet fully tackled challenge as

https://doi.org/10.1021/acsaelm.1c01348
ACS Appl. Electron. Mater. 2022, 4, 1703−1714

material selective deposition on relevant patterned substrate is sought. Such an issue is caused by the limited thickness of the employed passivation film and the ASD film isotropic growth character, whose deposition is typically carried out by ALD or CVD.[66] On one hand, a monolayer-thick blocking film is desired to avoid poisoning of the growth surface at the pattern's feature interfaces. On the other hand, the lateral expansion of the deposited material could be hindered, or even completely prevented, if a passivation layer as thick as the target ASD film is employed. Therefore, it appears clear that the "monolayer trade-off" between growth inhibition selectivity and lateral overgrowth suppression poses a clear challenge for area deactivation ASD schemes at technology-relevant nanoscale. It is worth remarking that this sort of limitation is virtually shared by every ASD approach that relies on a passivation layer, regardless of the blocking layer nature (e.g., SAMs, SMIs, gas/plasma formed) as well as by strategies exploiting substrate inherent ALD selectivity.

CONCLUSIONS

In this study, ASD is tested on unprecedented scaled-down Cu/SiO_2 patterns with SiO_2 spacings as small as 10 nm. It has been demonstrated that Cu passivation by ODT-derived SAM enables the selective deposition of a hafnium nitride film thicker than 5 nm on SiO_2 on both 50 nm HP and 10 nm CD patterns. Post-ALD top-down SEM on the 50 nm HP lines was used to characterize and quantify different aspects of the ongoing defect formation mechanisms on the metal lines, confirming that a process temperature as low as 100 °C was fundamental to mitigate ASD defectivity. At this temperature, the nanoparticle generation rate was strongly hampered, and their growth was seemingly suppressed. No ALD inhibition was observed on the TaN barrier because of the poor thiol−Ta interaction.

As ASD had been attempted on sub-10 nm features, relevant insights over the SAM-enabled selective material deposition were obtained. Upon ODT coating, these structures were investigated by pulsed force AFM, proving the confinement of the SAM on the metallic lines. Consequently, the blocking layer was not observed to interfere with the ASD on 10 nm-wide SiO_2 spacings. These findings provided a definitive proof that relatively bulky SAM precursors, such as long alkyl chain ODT, can be employed to selectively passivate sub-10 nm patterns.

In conclusion, the Article highlights the "monolayer trade-off" between nucleation inhibition selectivity and lateral overgrowth suppression, which plays a key role at the relevant nanoscale. On aggressively scaled-down patterns, both aspects are crucial to enable ASD because undesired protrusion of the passivation layer is more detrimental on a smaller and smaller GA and unwanted ASD film expansion sequestrates a relatively larger portion of the NGA. Overcoming the later overgrowth challenge is going to determine the feasibility of ASD in semiconductor manufacturing processing, together with defect mitigation.

ASSOCIATED CONTENT

Supporting Information

The Supporting Information is available free of charge at https://pubs.acs.org/doi/10.1021/acsaelm.1c01348.

RBS investigation of hafnium nitride ALD on Cu, SiO_2, and TaN upon ALD; 10 nm pattern adhesion force maps prior to and upon ODT; hafnium nitride thickness versus ALD cycles; SEM of passivated blanket Cu and 50 nm Cu/SiO_2 upon ALD; ToF-SIMS measurements on Cu, SiO_2, and TaN prior to and upon ALD; SEM of passivated 50 nm patterns upon ALD; SAM thickness on 50 and 24 nm-wide Cu lines (PDF)

AUTHOR INFORMATION

Corresponding Author

Silvia Armini − *Semiconductor Technology and System, Imec, B-3001 Leuven, Belgium;* orcid.org/0000-0003-0578-3422; Email: silvia.armini@imec.be

Authors

Mattia Pasquali − *Department of Chemistry, Faculty of Science, KU Leuven, B-3001 Leuven, Belgium; Semiconductor Technology and System, Imec, B-3001 Leuven, Belgium;* orcid.org/0000-0002-1309-1082

Patrick Carolan − *Semiconductor Technology and System, Imec, B-3001 Leuven, Belgium*

Stefanie Sergeant − *Semiconductor Technology and System, Imec, B-3001 Leuven, Belgium;* orcid.org/0000-0001-9923-0903

Johan Meersschaut − *Semiconductor Technology and System, Imec, B-3001 Leuven, Belgium*

Valentina Spampinato − *Semiconductor Technology and System, Imec, B-3001 Leuven, Belgium;* orcid.org/0000-0003-3225-6740

Thierry Conard − *Semiconductor Technology and System, Imec, B-3001 Leuven, Belgium*

Alessandro Viva − *Semiconductor Technology and System, Imec, B-3001 Leuven, Belgium*

Stefan De Gendt − *Department of Chemistry, Faculty of Science, KU Leuven, B-3001 Leuven, Belgium; Semiconductor Technology and System, Imec, B-3001 Leuven, Belgium*

Complete contact information is available at: https://pubs.acs.org/10.1021/acsaelm.1c01348

Notes

The authors declare no competing financial interest.

ACKNOWLEDGMENTS

The project has been funded by Imec's Industrial Affiliation Program on Nano-Interconnects. The authors acknowledge Imec's p-line for support in manufacturing of the patterned test wafers, Sebastiaan J. F. Herregods for valuable support in developing the hafnium nitride ALD process, Jan-Willem J. Clerix for coding the script used to compute the PSDs, and Hans Billington and Inge Manders for their help with the SEM measurements.

REFERENCES

(1) Clark, R.; Tapily, K.; Yu, K. H.; Hakamata, T.; Consiglio, S.; O'Meara, D.; Wajda, C.; Smith, J.; Leusink, G. Perspective: New Process Technologies Required for Future Devices and Scaling. *APL Mater.* **2018**, *6* (5), 058203.

(2) Schuegraf, K.; Abraham, M. C.; Brand, A.; Naik, M.; Thakur, R. Semiconductor Logic Technology Innovation to Achieve Sub-10 Nm Manufacturing. *IEEE J. Electron Devices Soc.* **2013**, *1* (3), 66−75.

(3) Kim, H.; Lee, H. B. R.; Maeng, W. J. Applications of Atomic Layer Deposition to Nanofabrication and Emerging Nanodevices. *Thin Solid Films* **2009**, *517* (8), 2563−2580.

(4) Lee, H.-B.-R. The Era of Atomic Crafting. *Chem. Mater.* **2019**, *31* (5), 1471−1472.
(5) Parsons, G. N.; Clark, R. D. Area-Selective Deposition: Fundamentals, Applications, and Future Outlook. *Chem. Mater.* **2020**, *32* (12), 4920−4953.
(6) Yarbrough, J.; Shearer, A. B.; Bent, S. F. Next Generation Nanopatterning Using Small Molecule Inhibitors for Area-Selective Atomic Layer Deposition. *J. Vac. Sci. Technol. A Vacuum, Surfaces, Film.* **2021**, *39* (2), 021002.
(7) Parsons, G. N. Functional Model for Analysis of ALD Nucleation and Quantification of Area-Selective Deposition. *J. Vac. Sci. Technol. A* **2019**, *37* (2), 020911.
(8) Mackus, A. J. M.; Merkx, M. J. M.; Kessels, W. M. M. From the Bottom-Up: Toward Area-Selective Atomic Layer Deposition with High Selectivity. *Chem. Mater.* **2019**, *31* (1), 2−12.
(9) Mackus, A. J. M.; Bol, A. A.; Kessels, W. M. M. The Use of Atomic Layer Deposition in Advanced Nanopatterning. *Nanoscale* **2014**, *6* (19), 10941−10960.
(10) Lu, J.; Low, K.-B.; Lei, Y.; Libera, J. A.; Nicholls, A.; Stair, P. C.; Elam, J. W. Toward Atomically-Precise Synthesis of Supported Bimetallic Nanoparticles Using Atomic Layer Deposition. *Nat. Commun.* **2014**, *5* (1), 3264.
(11) Metrology Session. In *3rd Area Selective Deposition Workshop (ASD2018)*, April 29 to May 1, 2018, North Carolina State University, Raleigh, NC, USA.
(12) Chen, R.; Kim, H.; McIntyre, P.; Bent, S. Investigation of Self-Assembled Monolayer Resists for Hafnium Dioxide Atomic Layer Deposition. *Chem. Mater.* **2005**, *17* (3), 536−544.
(13) Lee, H.-B.-R.; Bent, S. F. Nanopatterning by Area-Selective Atomic Layer Deposition. In *Atomic Layer Deposition of Nanostructured Materials*; Pinna, N., Knez, M., Eds.; Wiley-VCH Verlag GmbH & Co. KGaA, 2012; pp 193−225.
(14) Gladfelter, W. L. Selective Metalization by Chemical Vapor Deposition. *Chem. Mater.* **1993**, *5* (10), 1372−1388.
(15) George, S. Atomic Layer Deposition: An Overview. *Chem. Rev.* **2010**, *110* (1), 111−131.
(16) Gusev, E. P.; Cabral, C.; Copel, M.; D'Emic, C.; Gribelyuk, M. Ultrathin HfO_2 Films Grown on Silicon by Atomic Layer Deposition for Advanced Gate Dielectrics Applications. *Microelectron. Eng.* **2003**, *69* (2), 145−151.
(17) Mameli, A.; Merkx, M. J. M.; Karasulu, B.; Roozeboom, F.; Kessels, E. W. M. M.; Mackus, A. J. M. Area-Selective Atomic Layer Deposition of SiO_2 Using Acetylacetone as a Chemoselective Inhibitor in an ABC-Type Cycle. *ACS Nano* **2017**, *11* (9), 9303−9311.
(18) Hashemi, F. S. M.; Prasittichai, C.; Bent, S. F. Self-Correcting Process for High Quality Patterning by Atomic Layer Deposition. *ACS Nano* **2015**, *9* (9), 8710−8717.
(19) Zyulkov, I.; Krishtab, M.; De Gendt, S.; Armini, S. Selective Ru ALD as a Catalyst for Sub-Seven-Nanometer Bottom-Up Metal Interconnects. *ACS Appl. Mater. Interfaces* **2017**, *9* (36), 31031−31041.
(20) Wojtecki, R.; Mettry, M.; Fine Nathel, N. F.; Friz, A.; De Silva, A.; Arellano, N.; Shobha, H. Fifteen Nanometer Resolved Patterns in Selective Area Atomic Layer Deposition—Defectivity Reduction by Monolayer Design. *ACS Appl. Mater. Interfaces* **2018**, *10* (44), 38630−38637.
(21) Kim, W. H.; Minaye Hashemi, F. S.; Mackus, A. J. M.; Singh, J.; Kim, Y.; Bobb-Semple, D.; Fan, Y.; Kaufman-Osborn, T.; Godet, L.; Bent, S. F. A Process for Topographically Selective Deposition on 3D Nanostructures by Ion Implantation. *ACS Nano* **2016**, *10* (4), 4451−4458.
(22) Färm, E.; Kemell, M.; Ritala, M.; Leskelä, M. Selective-Area Atomic Layer Deposition with Microcontact Printed Self-Assembled Octadecyltrichlorosilane Monolayers as Mask Layers. *Thin Solid Films* **2008**, *517* (2), 972−975.
(23) Krishtab, M.; Armini, S.; Meersschaut, J.; Gendt, S. De; Ameloot, R. Cyclic Plasma Halogenation of Amorphous Carbon for Defect-Free Area-Selective Atomic Layer Deposition of Titanium Oxide. *ACS Appl. Mater. Interfaces* **2021**, *13* (27), 32381−32392.
(24) Bobb-Semple, D.; Nardi, K. L.; Draeger, N.; Hausmann, D. M.; Bent, S. F. Area-Selective Atomic Layer Deposition Assisted by Self-Assembled Monolayers: A Comparison of Cu, Co, W, and Ru. *Chem. Mater.* **2019**, *31* (5), 1635−1645.
(25) Merkx, M. J. M.; Vlaanderen, S.; Faraz, T.; Verheijen, M. A.; Kessels, W. M. M.; Mackus, A. J. M. Area-Selective Atomic Layer Deposition of TiN Using Aromatic Inhibitor Molecules for Metal/Dielectric Selectivity. *Chem. Mater.* **2020**, *32* (18), 7788−7795.
(26) Soethoudt, J.; Tomczak, Y.; Meynaerts, B.; Chan, B. T.; Delabie, A. Insight into Selective Surface Reactions of Dimethylamino-Trimethylsilane for Area-Selective Deposition of Metal, Nitride, and Oxide. *J. Phys. Chem. C* **2020**, *124* (13), 7163−7173.
(27) Pasquali, M.; De Gendt, S.; Armini, S. Area-Selective Deposition by a Combination of Organic Film Passivation and Atomic Layer Deposition. *ECS Trans.* **2019**, *92* (3), 25−32.
(28) Zyulkov, I.; Voronina, E.; Krishtab, M.; Voloshin, D.; Chan, B. T.; Mankelevich, Y.; Rakhimova, T.; Armini, S.; De Gendt, S. Area-Selective Ru ALD by Amorphous Carbon Modification Using H Plasma: From Atomistic Modeling to Full Wafer Process Integration. *Mater. Adv.* **2020**, *1* (8), 3049.
(29) Vallat, R.; Gassilloud, R.; Salicio, O.; El Hajjam, K.; Molas, G.; Pelissier, B.; Vallée, C. Area Selective Deposition of TiO_2 by Intercalation of Plasma Etching Cycles in PEALD Process: A Bottom up Approach for the Simplification of 3D Integration Scheme. *J. Vac. Sci. Technol. A* **2019**, *37* (2), 20918.
(30) Ulman, A. Formation and Structure of Self-Assembled Monolayers. *Chem. Rev.* **1996**, *96* (4), 1533−1554.
(31) Porter, M. D.; Bright, T. B.; Allara, D. L.; Chidsey, C. E. D. Spontaneously Organized Molecular Assemblies. 4. Structural Characterization of n-Alkyl Thiol Monolayers on Gold by Optical Ellipsometry, Infrared Spectroscopy, and Electrochemistry. *J. Am. Chem. Soc.* **1987**, *109* (12), 3559−3568.
(32) Zheng, L.; He, W.; Spampinato, V.; Franquet, A.; Sergeant, S.; Gendt, S. De; Armini, S. Area-Selective Atomic Layer Deposition of TiN Using Trimethoxy(Octadecyl)Silane as a Passivation Layer. *Langmuir* **2020**, *36* (44), 13144−13154.
(33) Hashemi, F.; Bent, S. Sequential Regeneration of Self-Assembled Monolayers for Highly Selective Atomic Layer Deposition. *Adv. Mater. Interfaces* **2016**, *3* (21), 1600464.
(34) Love, C.; Estroff, L.; Kriebel, J.; Nuzzo, R. G.; Whitesides, G. M. Self-Assembled Monolayers of Thiolates on Metals as a Form of Nanotechnology. *Chem. Rev.* **2005**, *105* (4), 1103−1170.
(35) Kim, H. G.; Kim, M.; Gu, B.; Khan, M. R.; Ko, B. G.; Yasmeen, S.; Kim, C. S.; Kwon, S. H.; Kim, J.; Kwon, J.; Jin, K.; Cho, B.; Chun, J.-S.; Shong, B.; Lee, H.-B.-R. Effects of Al Precursors on Deposition Selectivity of Atomic Layer Deposition of Al_2O_3 Using Ethanethiol Inhibitor. *Chem. Mater.* **2020**, *32* (20), 8921−8929.
(36) Soethoudt, J.; Grillo, F.; Marques, E. A.; van Ommen, J. R.; Tomczak, Y.; Nyns, L.; Van Elshocht, S.; Delabie, A. Diffusion-Mediated Growth and Size-Dependent Nanoparticle Reactivity during Ruthenium Atomic Layer Deposition on Dielectric Substrates. *Adv. Mater. Interfaces* **2018**, *5* (24), 1800870.
(37) Zyulkov, I.; Madhiwala, V.; Voronina, E.; Snelgrove, M.; Bogan, J.; O'Connor, R.; De Gendt, S.; Armini, S. Area-Selective ALD of Ru on Nanometer-Scale Cu Lines through Dimerization of Amino-Functionalized Alkoxy Silane Passivation Films. *ACS Appl. Mater. Interfaces* **2020**, *12* (4), 4678−4688.
(38) Pasquali, M.; Sergeant, S.; Conard, T.; Spampinato, V.; Viva, A.; De Gendt, S.; Armini, S. Nanomechanical Characterization of Organic Surface Passivation Films on 50 Nm Patterns during Area-Selective Deposition. *ACS Appl. Electron. Mater.* **2021**, *3* (6), 2622−2630.
(39) Cappella, B.; Dietler, G. Force-Distance Curves by Atomic Force Microscopy. *Surf. Sci. Rep.* **1999**, *34* (1−3), 1−104.
(40) Pasquali, M.; De Gendt, S.; Armini, S. Understanding the Impact of Cu Surface Pre-Treatment on Octadecanethiol-Derived

https://doi.org/10.1021/acsaelm.1c01348
ACS Appl. Electron. Mater. 2022, 4, 1703−1714

Self-Assembled Monolayer as a Mask for Area-Selective Deposition. *Appl. Surf. Sci.* **2021**, *540*, 148307.
(41) Meersschaut, J.; Vandervorst, W. High-Throughput Ion Beam Analysis at Imec. *Nucl. Instruments Methods Phys. Res. Sect. B Beam Interact. with Mater. Atoms* **2017**, *406*, 25−29.
(42) *NIST X-ray Photoelectron Spectroscopy (XPS) Database*; https://srdata.nist.gov/xps (accessed 2021-02-01); DOI: 10.18434/T4T88K.
(43) Shchukarev, A. V.; Korolkov, D. V. XPS Study of Group IA Carbonates. *Cent. Eur. J. Chem.* **2004**, *2* (2), 347−362.
(44) Laibinis, P.; Whitesides, G. ω-Terminated Alkanethiolate Monolayers on Surfaces of Copper, Silver, and Gold Have Similar Wettabilities. *J. Am. Chem. Soc.* **1992**, *114* (6), 1990−1995.
(45) Kim, H.; Colavita, P. E.; Paoprasert, P.; Gopalan, P.; Kuech, T. F.; Hamers, R. J. Grafting of Molecular Layers to Oxidized Gallium Nitride Surfaces via Phosphonic Acid Linkages. *Surf. Sci.* **2008**, *602* (14), 2382−2388.
(46) Rechmann, J.; Krzywiecki, M.; Erbe, A. Carbon−Sulfur Bond Cleavage During Adsorption of Octadecane Thiol to Copper in Ethanol. *Langmuir* **2019**, *35* (21), 6888−6897.
(47) Deroubaix, G.; Marcus, P. X-ray Photoelectron Spectroscopy Analysis of Copper and Zinc Oxides and Sulphides. *Surf. Interface Anal.* **1992**, *18* (1), 39−46.
(48) Powell, C. J.; Jablonski, A. Evaluation of Calculated and Measured Electron Inelastic Mean Free Paths near Solid Surfaces. *J. Phys. Chem. Ref. Data* **1999**, *28* (1), 19−62.
(49) Su, C.; Shi, J.; Hu, Y.; Hu, S.; Ma, J. *Method and Apparatus of Using Peak Force Tapping Mode to Measure Physical Properties of a Sample*. US 9291640 B2, 2008.
(50) O'Haver, T. *A Pragmatic Introduction to Signal Processing*; https://terpconnect.umd.edu/~toh/spectrum/ (accessed 2021-06-29).
(51) Becker, J. S.; Kim, E.; Gordon, R. G. Atomic Layer Deposition of Insulating Hafnium and Zirconium Nitrides. *Chem. Mater.* **2004**, *16* (18), 3497−3501.
(52) Fix, R.; Gordon, R. G.; Hoffman, D. M. Chemical Vapor Deposition of Titanium, Zirconium, and Hafnium Nitride Thin Films. *Chem. Mater.* **1991**, *3* (6), 1138−1148.
(53) Xu, Y.; Musgrave, C. B. Atomic Layer Deposition of Hafnium Nitrides Using Ammonia and Alkylamide Precursors. *Chem. Phys. Lett.* **2005**, *407* (4−6), 272−275.
(54) Maex, K.; Baklanov, M. R.; Shamiryan, D.; Iacopi, F.; Brongersma, S. H.; Yanovitskaya, Z. S. Low Dielectric Constant Materials for Microelectronics. *J. Appl. Phys.* **2003**, *93* (11), 8793−8841.
(55) Mackus, A. J. M.; MacIsaac, C.; Kim, W.-H.; Bent, S. F. Incomplete Elimination of Precursor Ligands during Atomic Layer Deposition of Zinc-Oxide, Tin-Oxide, and Zinc-Tin-Oxide. *J. Chem. Phys.* **2017**, *146* (5), 052802.
(56) Hashemi, F.; Birchansky, B.; Bent, S. Selective Deposition of Dielectrics: Limits and Advantages of Alkanethiol Blocking Agents on Metal−Dielectric Patterns. *ACS Appl. Mater. Interfaces* **2016**, *8* (48), 33264−33272.
(57) Färm, E.; Vehkamäki, M.; Ritala, M.; Leskelä, M. Passivation of Copper Surfaces for Selective-Area ALD Using a Thiol Self-Assembled Monolayer. *Semicond. Sci. Technol.* **2012**, *27* (7), 074004.
(58) Bergsman, D. S.; Liu, T. L.; Closser, R. G.; Nardi, K. L.; Draeger, N.; Hausmann, D. M.; Bent, S. F. Formation and Ripening of Self-Assembled Multilayers from the Vapor-Phase Deposition of Dodecanethiol on Copper Oxide. *Chem. Mater.* **2018**, *30* (16), 5694−5703.
(59) Liu, T. L.; Nardi, K. L.; Draeger, N.; Hausmann, D. M.; Bent, S. F. Effect of Multilayer versus Monolayer Dodecanethiol on Selectivity and Pattern Integrity in Area-Selective Atomic Layer Deposition. *ACS Appl. Mater. Interfaces* **2020**, *12* (37), 42226−42235.
(60) Grillo, F.; Van Bui, H.; Moulijn, J. A.; Kreutzer, M. T.; van Ommen, J. R. Understanding and Controlling the Aggregative Growth of Platinum Nanoparticles in Atomic Layer Deposition: An Avenue to Size Selection. *J. Phys. Chem. Lett.* **2017**, *8* (5), 975−983.
(61) Grillo, F.; Moulijn, J. A.; Kreutzer, M. T.; van Ommen, J. R. Nanoparticle Sintering in Atomic Layer Deposition of Supported Catalysts: Kinetic Modeling of the Size Distribution. *Catal. Today* **2018**, *316*, 51−61.
(62) Dendooven, J.; Ramachandran, R. K.; Solano, E.; Kurttepeli, M.; Geerts, L.; Heremans, G.; Rongé, J.; Minjauw, M. M.; Dobbelaere, T.; Devloo-Casier, K.; Martens, J. A.; Vantomme, A.; Bals, S.; Portale, G.; Coati, A.; Detavernier, C. Independent Tuning of Size and Coverage of Supported Pt Nanoparticles Using Atomic Layer Deposition. *Nat. Commun. 2017 81* **2017**, *8* (1), 1−12.
(63) Clerix, J.-W. J.; Marques, E. A.; Soethoudt, J.; Grillo, F.; Pourtois, G.; van Ommen, J. R.; Delabie, A. Selectivity Enhancement for Ruthenium Atomic Layer Deposition in Sub-50 Nm Nanopatterns by Diffusion and Size-Dependent Reactivity. *Adv. Mater. Interfaces* **2021**, *8* (20), 2100846.
(64) Grillo, F.; Soethoudt, J.; Marques, E. A.; de Martín, L.; van Dongen, K.; van Ommen, J. R.; Delabie, A. Area-Selective Deposition of Ruthenium by Area-Dependent Surface Diffusion. *Chem. Mater.* **2020**, *32* (22), 9560−9572.
(65) Chopra, S.; Zhang, Z.; Kaihlanen, C.; Ekerdt, J. Selective Growth of Titanium Nitride on HfO_2 across Nanolines and Nanopillars. *Chem. Mater.* **2016**, *28* (14), 4928−4934.
(66) Ras, R. H. A.; Sahramo, E.; Malm, J.; Raula, J.; Karppinen, M. Blocking the Lateral Film Growth at the Nanoscale in Area-Selective Atomic Layer Deposition. *J. Am. Chem. Soc.* **2008**, *130* (34), 11252−11253.
(67) Krotil, H.-U.; Stifter, T.; Waschipky, H.; Weishaupt, K.; Hild, S.; Marti, O. Pulsed Force Mode: A New Method for the Investigation of Surface Properties. *Surf. Interface Anal.* **1999**, *27* (5−6), 336−340.
(68) Rosa-Zeiser, A.; Weilandt, E.; Hild, S.; Marti, O. Simultaneous Measurement of Elastic, Electrostatic and Adhesive Properties by Scanning Force Microscopy: Pulsed-Force Mode Operation. *Meas. Sci. Technol.* **1997**, *8* (11), 1333−1338.
(69) Rico, F.; Su, C.; Scheuring, S. Mechanical Mapping of Single Membrane Proteins at Submolecular Resolution. *Nano Lett.* **2011**, *11* (9), 3983−3986.
(70) Krieg, M.; Fläschner, G.; Alsteens, D.; Gaub, B. M.; Roos, W. H.; Wuite, G. J. L.; Gaub, H. E.; Gerber, C.; Dufrêne, Y. F.; Müller, D. J. Atomic Force Microscopy-Based Mechanobiology. *Nat. Rev. Phys.* **2019**, *1* (1), 41−57.